J. Fluid Mech., page 1 of 23. © Cambridge University Press 2012
doi:10.1017/jfm.2012.78

The attraction between a flexible filament and a point vortex

Silas Alben†

School of Mathematics, Georgia Institute of Technology, Atlanta, GA 30332-0160, USA

(Received 6 September 2011; revised 3 December 2011; accepted 4 February 2012)

We determine the inviscid dynamics of a point vortex in the vicinity of a flexible filament. For a wide range of filament bending rigidities, the filament is attracted to the point vortex, which generally moves tangentially to it. We find evidence that the point vortex collides with the filament at a critical time, with the separation distance tending to zero like a square root of temporal distance from the critical time. Concurrent with the collision, we find divergences of pressure loading on the filament, filament vortex sheet strength, filament curvature and velocity. We derive the corresponding power laws using the governing equations.

Key words: flow–structure interactions, vortex dynamics, vortex interactions

1. Introduction

The interaction between solid bodies and vortices is important in many areas of biology, physics and engineering. Bluegill sunfish can swim using both the dorsal fin and the caudal fin in a tandem configuration. Vorticity shed from the dorsal fin moves downstream and contacts the caudal fin, altering the flow around it and the forces on it (Drucker & Lauder 2001). Thrust forces depend sensitively on the relative phase between the fins, according to flexible foil simulations by Akhtar *et al.* (2007). Similar thrust enhancement can also occur for fish swimming in the vortical wakes of static obstacles (Liao *et al.* 2003; Beal *et al.* 2006). Models and simulations have identified optimal swimming motions relative to vortices, for rigid and flexible foils swimming in a von Kármán vortex street wake (Streitlien, Triantafyllou & Triantafyllou 1996; Alben 2008*a*, 2010). The interactions of passive flexible bodies with vortex wakes can illuminate the underlying physics of these systems, and indicate energy-saving motions (Ristroph & Zhang 2008; Eldredge & Pisani 2008; Manela & Howe 2009; Alben 2009). Vortices shed from aircraft structures can have important interactions with other aircraft structures downstream; studies of these interactions are reviewed by Doligalski, Smith & Walker (1994).

In this work we study a fundamental interaction between a vortex and a simple passive body: a flexible filament. Our interest is mainly to understand the generic coupled dynamics of a vortex and a passive flexible surface. We consider a point vortex in a purely inviscid flow, and therefore set aside many complicated and interesting phenomena associated with viscosity. For example, when a vortex impinges on a solid surface, a viscous boundary layer may separate from the surface, leading

† Email address for correspondence: alben@math.gatech.edu

to the creation of additional vortices which interact with the original impinging vortex. Such interactions for rigid bodies have been reviewed by Rockwell (1998). The present work, which solves for the inviscid interaction between a point vortex and a flexible body, seems like a natural starting place for a general understanding of interactions between a vortex and a flexible body.

Inviscid interactions of vortices with rigid walls of various geometries can be solved using image systems and more generally, the Kirchhoff–Routh path function (Milne-Thomson 1968; Saffman 1992; Crowdy & Marshall 2006). Recently there have been theoretical and computational studies of the dynamics of interacting systems of point vortices and moving rigid bodies (Kadtke & Novikov 1993; Shashikanth *et al.* 2002; Borisov, Mamaev & Ramodanov 2007; Kanso & Oskouei 2008; Protas 2008; Vankerschaver, Kanso & Marsden 2009; Roenby & Aref 2010). In Alben (2011), two simple solutions were given for the motion of a vortex near a flexible wall. In these solutions, the vortex moves steadily along the wall, and induces an outward bump on it. The wall is either an infinite straight line, or a circle in the undeformed state, and deforms as a surface on an elastic foundation, with or without membrane tension along the surface. For the circular wall, the distance from the wall to the vortex is a key parameter. The force on the wall and its deformation are proportional to the inverse cube of the distance to the point vortex. That work was restricted to steady, small-magnitude travelling-wave deformations. In the present work, we extend to general unsteady dynamics with a different body which is more tractable computationally: a finite flexible filament.

In § 2, we present the system of equations describing the coupled dynamics of the filament and point vortex. In § 3 we describe our numerical method, adaptive in space and time, for computing solutions. Section 4 presents simulations for a variety of filament rigidities and initial vortex positions. We depict the variation in dynamics from the periodic orbits the vortex makes around a rigid filament, to the finite-time collisions of a vortex with a flexible filament. We determine the asymptotic power-law scalings of flow and shape quantities leading up to the collisions. Section 5 reviews the main results and discusses future directions.

2. Filament–vortex model

We consider an inextensible flexible filament in an unbounded two-dimensional inviscid fluid. Figure 1 shows the filament and point vortex in a typical configuration. The filament has length L, uniform thickness h, uniform mass per unit area ρ_s, and uniform bending rigidity B. The fluid has mass per unit area ρ_f. At the initial time, $t = 0$, a point vortex with circulation Γ is placed at position $x_0 + iy_0$. The filament is initially in its equilibrium state: flat and horizontal. In forward time, the filament deflects under fluid pressure loading, according to the unsteady elastica equation, given in dimensionless form as

$$R_1 \partial_{tt}\zeta(s,t) = -R_2 \partial_s(\partial_s \kappa(s,t) \mathrm{i} e^{\mathrm{i}\theta(s,t)}) + \partial_s(T(s,t) e^{\mathrm{i}\theta(s,t)}) - [p](s,t) \mathrm{i} e^{\mathrm{i}\theta(s,t)}. \quad (2.1)$$

Here ζ is the filament position in the complex plane, s is arclength along the filament, θ and κ are the filament tangent angle and curvature, respectively, T is the tension which maintains inextensibility, and $[p]$ is the pressure jump across the filament. The unit tangent and normal to the fibre are $e^{\mathrm{i}\theta(s,t)}$ and $ie^{\mathrm{i}\theta(s,t)}$, respectively.

In (2.1), we have non-dimensionalized length by the filament half-length, $L/2$ (the factor of 2 simplifies a subsequent integral equation), time by $L^2/4\Gamma$ and mass by $\rho_f L^2/4$. All quantities are non-dimensionalized by these choices. The dimensionless

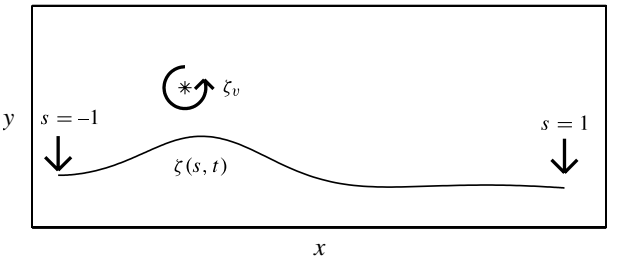

FIGURE 1. Schematic diagram of the point vortex ζ_v and the filament $\zeta(s,t)$, with arclength s ranging from -1 at the clamped end to 1 at the free end.

filament mass density is

$$R_1 = \frac{2\rho_s h}{\rho_f L}. \tag{2.2}$$

We work in the limit of a very thin filament, $h \to 0$, so we set R_1 to zero, which simplifies the problem. Thus, all of the inertia resides in the fluid. The dimensionless filament bending rigidity is

$$R_2 = \frac{2B}{\rho_f \Gamma^2 L}. \tag{2.3}$$

R_2 is a ratio of bending rigidity and fluid pressure forces, and is one of the main parameters of interest in this work. The filament is clamped at the origin with zero tangent angle at one end (with arclength $s=-1$) and is free at the other end ($s=1$):

$$\zeta(-1,t)=0; \quad \theta(-1,t)=0; \quad \kappa(1,t)=0; \quad \partial_s\kappa(1,t)=0. \tag{2.4}$$

Free–free boundary conditions are also possible, but are somewhat more challenging for convergence of the iterative method used in our simulations at certain times.

As the body moves in the fluid, the condition that fluid does not penetrate the body is enforced by posing a vortex sheet, of strength $\gamma(s,t)$, on the body (Saffman 1992). This 'singularity method' is similar to classical panel methods for potential flows past aircraft (Katz & Plotkin 2001). The condition that fluid does not penetrate the filament determines γ. We equate the component of the fluid velocity normal to the filament to the component of the filament's velocity normal to itself:

$$\mathrm{Re}\left(\frac{\mathrm{e}^{\mathrm{i}\theta(s,t)}}{2\pi} \fint \frac{\gamma(s',t)}{\zeta(s,t)-\zeta(s',t)}\,\mathrm{d}s'\right) + \mathrm{Re}\left(\frac{\mathrm{e}^{\mathrm{i}\theta(s,t)}}{2\pi}\frac{1}{\zeta(s,t)-\zeta_v(t)}\right) = v(s,t). \tag{2.5}$$

In (2.5), the principal value integral on the left-hand side gives the normal component of fluid velocity induced by the vortex sheet. The second term on the left-hand side is the normal component of fluid velocity induced by the point vortex. The point vortex has position $\zeta_v(t)$, and moves simultaneously with the filament, as will be described shortly. The left-hand side of (2.5) is thus the component of the fluid velocity normal to the filament. On the right-hand side of (2.5) we have $v(s,t)$, which denotes the component of the filament's velocity normal to itself. Denoting the tangential component of filament velocity by $\tau(s,t)$, we have the decomposition

$$\tau(s,t) + iv(s,t) = \partial_t\zeta(s,t)\mathrm{e}^{-\mathrm{i}\theta(s,t)}. \tag{2.6}$$

The point vortex moves at the local fluid velocity induced by the bound vortex sheet:

$$\partial_t \bar{\zeta}_v = \frac{1}{2\pi \mathrm{i}} \int_{-1}^{1} \frac{\gamma(s,t)}{\zeta_v(t) - \zeta(s,t)} \, \mathrm{d}s. \tag{2.7}$$

The pressure jump across the filament may be derived in terms of γ, τ and the average tangential component of the flow speed at the filament which we denote by μ. Here μ is the sum of the tangential flow induced by the point vortex and the bound vortex sheet, which can be written in terms of γ:

$$\mu(s,t) = \mathrm{Im}\left(\frac{\mathrm{e}^{\mathrm{i}\theta(s,t)}}{2\pi} \fint \frac{\gamma(s',t)}{\zeta(s,t) - \zeta(s',t)} \, \mathrm{d}s' \right) + \mathrm{Im}\left(\frac{\mathrm{e}^{\mathrm{i}\theta(s,t)}}{2\pi} \frac{1}{\zeta(s,t) - \zeta_v(t)} \right). \tag{2.8}$$

The difference in pressure from the $+$ to the $-$ side of the filament is

$$\partial_t \gamma + \partial_s((\mu - \tau)\gamma) = \partial_s [p]_-^+ . \tag{2.9}$$

We use $+$ to denote the side towards which the filament normal $\hat{\boldsymbol{n}}$ is directed, and $-$ for the other side. Equation (2.9) is derived starting with the Euler equation at a point with fixed arclength on the filament. The derivation is given in appendix A.

Equations (2.1), (2.5), (2.7) and (2.9) are solved numerically for the dynamics of the filament and point vortex for $t > 0$. At $t = 0$, the filament is flat and horizontal, with zero velocity. The clamped end is at $z = 0$ and the free end is at $z = 2$. The point vortex is initially located at $\zeta_v(0) = x_0 + \mathrm{i}y_0$. The initial value of γ is then determined by (2.5). The initial velocity of the point vortex is then given by (2.7).

3. Numerical method

We use an implicit numerical scheme, which has good stability properties and is more straightforward to formulate than an explicit scheme for our equations. Our time stepping is similar to that of Alben (2009). We use a second-order backward-differentiation scheme, which is modified at the first time step to incorporate the initial conditions. The discretized versions of (2.1), (2.5), (2.7) and (2.9) are used to solve for κ, γ, $[p]$ and ζ_v at each time step. A damped Broyden iteration is used to solve the equations to a tolerance of 10^{-8} at each time step. In general, a smaller tolerance makes the iteration less likely to converge at later times in the simulations, when the condition number of the Jacobian matrix increases.

To resolve the dynamics of the point vortex close to the filament, our method is adaptive in time and space. We set the time step to resolve motions on the scale of the minimum distance from the point vortex to the filament. This is the typical length scale over which the flow and the filament deformation vary. If on successive time steps the point vortex moves more than a fixed fraction (typically 1/10) of the minimum distance to the filament, we halve the time step. This criterion allows us to resolve the filament–vortex dynamics.

We choose the spatial (s) grid for all quantities on the filament (ζ, γ, $[p]$, etc.) to resolve these quantities on the scale of the minimum distance from the point vortex to the filament. We define a smooth function $q(s)$ which maps $[-1, 1]$ to itself. We choose q such that a fixed (Lobatto) discretization of q corresponds to a discretization of s which is clustered near the point vortex. Specifically, we define

$$\frac{\mathrm{d}q}{\mathrm{d}s} = \frac{1}{c}\left(1 + \frac{1}{|\zeta_v - \zeta(s)|}\right). \tag{3.1}$$

We set $q(-1) = -1$, and choose c so that $q(1) = 1$:

$$c = \frac{1}{2}\int_{-1}^{1}\left(1 + \frac{1}{|\zeta_v - \zeta(s)|}\right)\mathrm{d}s. \tag{3.2}$$

Here $\mathrm{d}q/\mathrm{d}s$ is large at points on the filament where the distance from the filament to the point vortex is $\ll 1$, and at such points, $\mathrm{d}q/\mathrm{d}s$ is approximately the reciprocal of c times the distance to the point vortex. We discretize q with a Lobatto mesh (Boyd 2001). If the mesh is sufficiently fine, the spacing between the corresponding points in s satisfies

$$\Delta s \approx c|\zeta_v - \zeta(s)|\Delta q. \tag{3.3}$$

To ensure that the problem is spatially resolved, we require the spacing between points on the filament to be a small fraction of their distance from the point vortex. According to (3.3), this holds if $c\Delta q$ is a small fraction. For a Lobatto mesh with m points, $\Delta q \leqslant \pi/m$. If the point vortex is not too close to the filament, i.e. $|\zeta_v - \zeta(s)|$ is $O(1)$ for all s, then c is $O(1)$, so m of $O(1)$ (20, say) is sufficient to make $c\pi/m$ small.

The more important case is where the point vortex is close to the filament. For example, let $\zeta_v = i\epsilon$, $0 < \epsilon \ll 1$, and let $\zeta(s) = s$. The point vortex is thus a distance ϵ above the midpoint of a flat filament. Then by (3.2),

$$c = 2 + \log\left(2 + \epsilon^2 + 2\sqrt{1+\epsilon^2}\right) + 2\log\left(\frac{1}{\epsilon}\right). \tag{3.4}$$

To achieve good resolution now only requires that $m = O(\log(1/\epsilon))$, so the number of mesh points needed grows only logarithmically as the point vortex gets very close to the filament. A similar result holds for more general (curved) filament shapes, such as those for which only an $O(\epsilon)$ length of filament lies within $O(\epsilon)$ of the point vortex. Even though filaments become highly curved near the point vortex in our simulations, they maintain this property. In our simulations $m = 200$ gives good resolution for the smallest filament–vortex distances, which are $\sim 10^{-4}$.

Another advantage of (3.1) is that it can be used to write s-derivatives (as in (2.1)) analytically in terms of q-derivatives pre-multiplied by known functions of the filament shape. The q-derivatives can then be performed with spectrally accurate differentiation matrices, since all filament quantities are given on the fixed Lobatto mesh in the q domain.

4. Results

Simulations of the vortex-filament dynamics for the full range of filament rigidities are shown in the supplementary movie which accompanies this paper on the publisher's website (available at http://dx.doi.org/10.1017/jfm.2012.78).

4.1. *Stiff filaments*

We first consider the limiting case of a rigid filament, $R_2 \to \infty$. Here the motion of the point vortex can be found analytically using the Kirchhoff–Routh path function, and the solution is given by Milne-Thomson (1968). In figure 2, we show three of the infinite family of closed point-vortex trajectories; they are the three curves passing through $y_0 = 0.12, 0.25$ and 0.5, with $x_0 = 0.3$ in each case. The trajectories computed using our numerical method are shown as thin solid lines, and points on the trajectories corresponding to the analytical solutions, given parametrically by Milne-Thomson (1968), are shown with open symbols. The relative errors in position

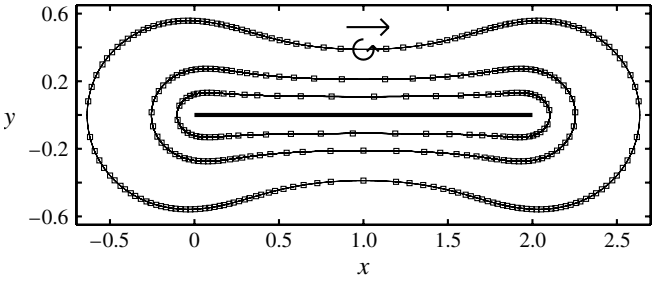

FIGURE 2. Rigid filament dynamics. The thin solid lines show three computed trajectories of point vortices about a nearly rigid filament (thick horizontal line segment, $R_2 = 10^5$), passing through $x_0 = 0.3$, $y_0 = 0.12, 0.25$ and 0.5. The open squares show points on the trajectories corresponding the analytical solutions of Milne-Thomson (1968). The arrow shows the direction of motion of the point vortex along the trajectories.

are less than 10^{-3}. Here we have used $m = 200$ and an initial time step $\Delta t = 0.05$, so the numerical parameters are similar to those used for subsequent results.

For R_2 large but finite, the filament undergoes small deflections about the rigid state. Here the numerical solutions are well-approximated by a regular asymptotic expansion, in integer powers of R_2^{-1}. For example, we expand the vertical deflection at the free end

$$y(1, t) = R_2^{-1} y_1(1, t) + R_2^{-2} y_2(1, t) + \cdots. \tag{4.1}$$

We now consider, for example, trajectories with $x_0 = 0.3$, $y_0 = 0.2$. In figure 3(*a*), the dashed line shows the vertical position of the point vortex (labelled y_v) in time as it makes six circuits around a nearly rigid filament ($R_2 = 10^6$). The solid lines (which nearly overlap) show, at the same times, the values of the vertical deflections of the filaments' free ends for three moderately stiff filaments: $R_2 = 100$, 300 and 1000. The values of the deflections are multiplied by R_2, so the solid lines approximate y_1 in (4.1) as $R_2 \to \infty$. These curves are well within the small deflection limit: the unscaled values of the deflections are uniformly less than 0.004 for these curves. When the point vortex passes around the free end of the filament (i.e. when the solid curves have a large negative slope), y_1 changes sign at the same instants as y_v, which means that the free end of the very stiff filament bends towards the point vortex.

In figure 3(*b*), we plot, for the same R_2 values as in (*a*), y minus the first-order term, scaled by R_2^2, i.e. the numerical approximation to y_2. High-frequency and rapidly decaying oscillations become visible. These oscillations are actually not part of the regular asymptotic expansion (4.1). They are associated with the initial conditions, and decay as the filament–vortex system tends to its periodic dynamics, from which the initial conditions deviate. The oscillations have initial amplitude $\sim R_2^{-1}$, a decay rate $\sim R_2^2$ and a frequency $\sim\sqrt{R_2}$. This last scaling is visually verified by figure 3(*c*), which plots the curves from (*b*) with time multiplied by $\sqrt{R_2}$. We also add the curve for $R_2 = 30$. With this scaling of time, the curves' temporal wavelengths agree closely. Returning now to figure (*b*), we find that after the oscillations have damped out, the curves overlap closely and slowly converge to a periodic curve, which is y_2.

The asymptotic expansion (4.1) can be explained simply, from (2.1). The pressure jump term is $O(1)$ at leading order due to the point vortex of circulation unity. This balances a bending rigidity term which is a product of R_2 and derivatives of deflection,

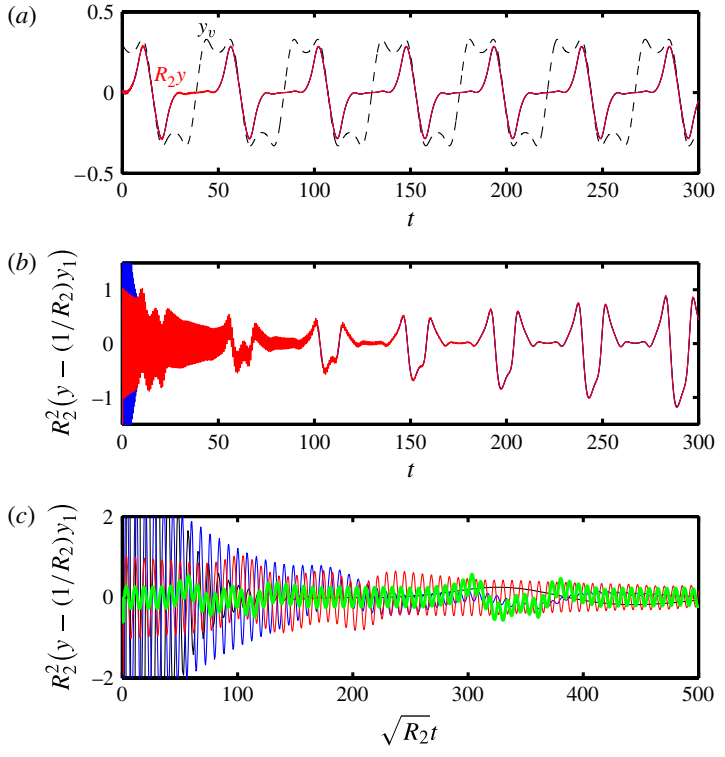

FIGURE 3. (Colour online available at journals.cambridge.org/flm) Deflections of nearly rigid filaments. (*a*) The dashed line gives the vertical position of the point vortex for a nearly rigid filament ($R_2 = 10^6$). The solid lines give the vertical positions of filaments' free ends, scaled by stiffness parameter R_2, for three values of R_2: 100 (medium grey or red), 300 (dark grey or blue) and 1000 (black). (*b*) The vertical positions of the filaments' free ends, minus the first-order solution $(1/R_2)y_1$, and scaled by R_2^2, for the same three values of R_2: 100, 300 and 1000. (*c*) The three curves from (*b*) ($R_2 = 100, 300, 1000$), plus a fourth curve ($R_2 = 30$, thick grey line or green), with time scaled by $\sqrt{R_2}$.

so the deflection resulting from an $O(1)$ pressure scales as R_2^{-1}. This deflection leads to an $O(R_2^{-1})$ pressure jump, which induces an $O(R_2^{-2})$ deflection, and so on.

The oscillations can be interpreted as resulting from the deviation of the initial conditions from periodic dynamics. The initial deflection (zero) is $O(R_2^{-1})$ from the deflection in the eventual periodic solution. For small deflections, equations (2.1), (2.5) and (2.9) can be reduced to a single linear integrodifferential equation for y, or two slightly shorter equations for y and γ:

$$R_2 \partial_x^5 y = -\partial_t \gamma - \partial_x \left(\frac{y_v}{2\pi \left[(x - x_v)^2 + y_v^2 \right]} \gamma \right), \tag{4.2}$$

$$\gamma = \frac{-1}{\pi} \frac{1}{\sqrt{1 - x^2}} \int_{-1}^{1} \frac{\sqrt{1 - x'^2}}{x - x'} \left(2\partial_t y + \frac{1}{\pi} \frac{x_v - x'}{(x_v - x')^2 + y_v^2} \right) \mathrm{d}x'. \tag{4.3}$$

Here we may consider the point vortex position (x_v, y_v) as fixed, because it evolves on a much longer ($O(1)$) time scale than the oscillations. Equations (4.2) and (4.3) are somewhat like a damped driven beam equation, except that there is a non-local

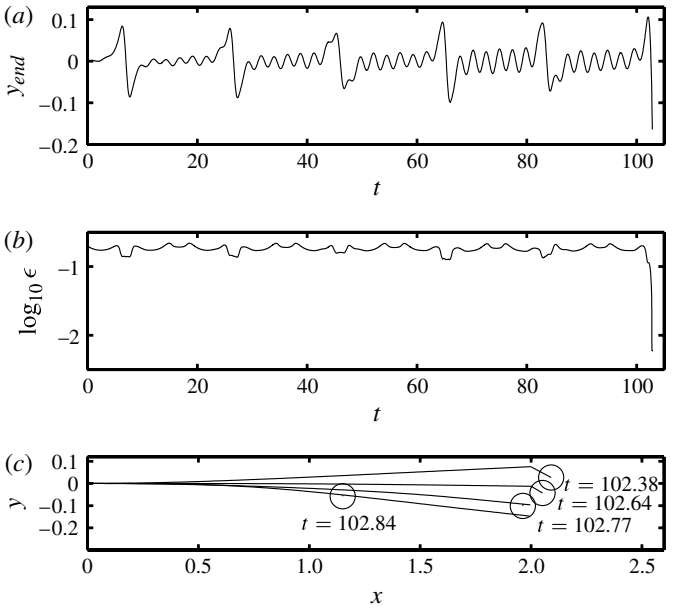

FIGURE 4. Vortex–filament dynamics for $R_2 = 10$, $x_0 = 0.3$ and $y_0 = 0.2$. (*a*) Free end deflection versus time. (*b*) Logarithm (base 10) of ϵ, the minimum distance from the point vortex to the filament, versus time. (*c*) Snapshots of the filament and point vortex (circle), with line segments connecting the two at corresponding times (shown adjacent to the point vortex), near the final time shown in (*b*).

integral operator (the 'aerofoil' operator) acting on the terms proportional to $\partial_t y$ and $\partial_{tt} y$. Thus, these terms are only loosely analogous to the damping and inertia terms in the classical damped driven beam equation (see Alben 2008*b*). However, the solutions to the classical equation are complex exponentials of time, with the same frequency $\sim\sqrt{R_2}$ as our transient oscillations. If we subtract from (4.2) and (4.3) the same equations, but written in terms of the periodic solution, the equations for the difference (i.e. the oscillatory term) are nearly the same. The equations for the difference are missing only the point vortex term in (4.3). The initial conditions for the oscillatory term are the difference between the $O(R_2^{-1})$ initial conditions for the periodic solution, and the zero initial conditions for the original solution. This explains the $O(R_2^{-1})$ initial amplitude of the oscillations.

4.2. *Flexible filaments*

We now consider a filament which is moderately flexible, $R_2 = 10$. In figure 4(*a*) we show the free end deflection versus time, as the point vortex makes about five circuits around the filament. The shape of the deflection time–trace curve is similar to that of the nearly rigid filament (figure 3*a*). The maxima again correspond to the passage of the vortex around the free end. The amplitude is of course larger now, and has a significant higher-frequency oscillation. Near $t = 102.6$, the distance between the point vortex and the filament decreases sharply. We now define $\epsilon(t)$ as the minimum distance from the point vortex to a point on the filament, as a function of time. In figure 4(*b*), we plot $\log_{10}\epsilon(t)$. There is a sharp decline shortly before the end time of the computation. At this time, the computation stagnates: it is unable to converge to a solution at the next time step. In figure 4(*c*), we show snapshots of the point vortex

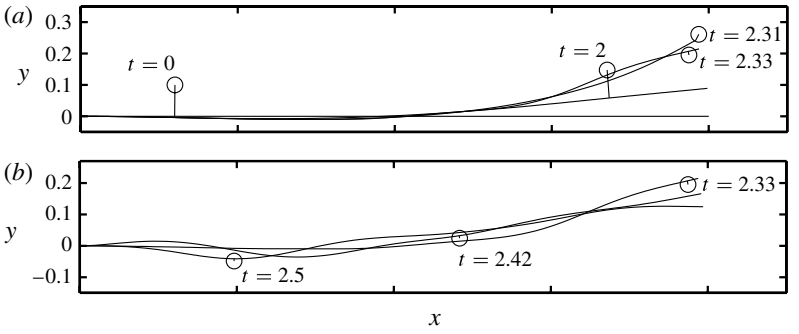

FIGURE 5. Vortex–filament dynamics for $R_2 = 0.3$, $x_0 = 0.3$ and $y_0 = 0.1$. Snapshots of the filament and point vortex (circle), with line segments connecting the two at corresponding times (shown adjacent to the point vortex). (*a*) Up to $t = 2.33$. (*b*) From $t = 2.33$ to $t = 2.5$.

and filament leading up to the end time. At $t = 102.38$, the point vortex (circle) is passing around the free end of the filament, which is still deflected upward because it was attracted to the point vortex as it passed over the upper surface of the filament, just before this time. At $t = 102.64$ and $t = 102.77$, the free end of the filament and the point vortex become much closer, while the point vortex passes to the lower side of the filament. There is apparently a strong attraction between the free end, with its inverse-square-root singularity in flow velocity and pressure, and the point vortex. At the final time, $t = 102.84$, the point vortex is near the middle of the lower surface of the filament. As it becomes nearer to the filament, its speed increases rapidly, because it induces larger vorticity on the filament, and it is closer to this vorticity (Alben 2011). Between $t = 102.77$ and 102.84, the speed of the vortex is more than 50 times its average speed between $t = 0$ and 102.77.

In figure 5 we show snapshots for a more flexible filament, $R_2 = 0.3$. In (*a*), the filament deflects upward as the point vortex passes around the free end, with bending more localized at the free end now. In (*b*), the filament flexes with multiply signed curvature, and the point vortex travels mainly tangentially to the filament, while the filament gradually approaches it. The final time of the computation is $t = 2.5$ and the distance between the point vortex and the filament is 7.3×10^{-3}.

We now decrease R_2 by a factor of 30, to 0.01, and show snapshots in figure 6. In (*a*), the filament deflects more rapidly upward toward the point vortex, forming a 'crest' along which the vortex travels. The final times of the computation are shown in (*b*). Between $t = 1.62$ and 1.68, the filament partially unbends, while the distance between the point vortex and the filament continually decreases. The computation ends at $t = 1.68$, before the vortex reaches the free end of the filament. At this time the distance between the point vortex and the filament is 5.8×10^{-3}.

In figure 7 we plot quantities for filaments with R_2 ranging over three orders of magnitude, from 4.2×10^{-3} to 4.2, which includes the values in figures 5 and 6. In (*a*), we plot $\epsilon(t)$, the minimum distance from the point vortex to filament. All of the simulations have $y_0 = 0.15$, so all of the curves emanate from 0.15 on the vertical axis. Moving from one curve to the next, from left to right, R_2 increases monotonically. Thus, $\epsilon(t)$ decreases most rapidly for the most flexible filaments. The thick dashed line corresponds to figure 6. For this curve and the three curves to the left of it, the simulation ends before the point vortex reaches the free end of the filament. For the 10 curves to the right of the dashed line, the simulation ends when the point

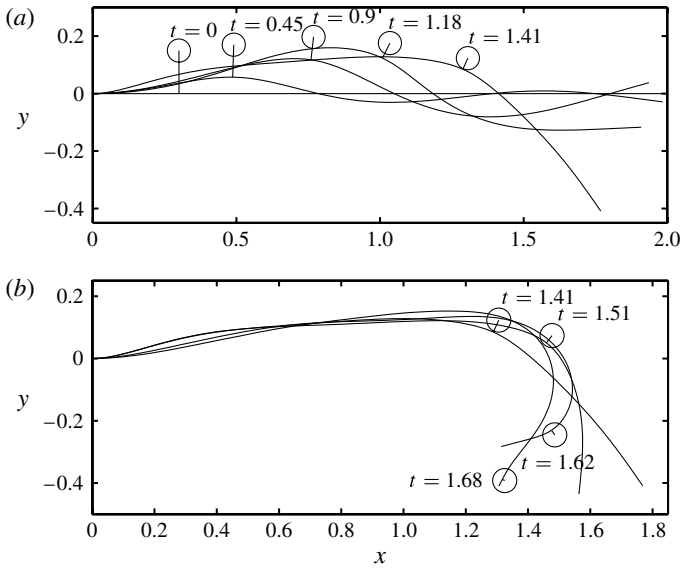

FIGURE 6. Vortex–filament dynamics for $R_2 = 0.01$, $x_0 = 0.3$ and $y_0 = 0.15$. Snapshots of the filament and point vortex (circle), with line segments connecting the two at corresponding times (shown adjacent to the point vortex). (*a*) Up to $t = 1.41$. (*b*) From $t = 1.41$ onwards.

vortex is very close to the free end. For the next 10 curves, the point vortex passes around the free end, and moves along the lower side of the filament back towards the clamped end, and in most cases reaches it. For the two stiffest filaments ($R_2 = 2.4$ and 4.2), the point vortex passes around the clamped end as well, and the simulation ends with the point vortex on the upper side of the filament. These observations are shown more clearly in (*b*), where ϵ is replotted against the arclength of the point on the filament nearest to the point vortex, which we denote s_v, instead of time. As the point vortex passes around the free end to the lower side of the filament, the arclength decreases from 1 down to -1, but here, to make the curves more visible, we use a monotonically increasing arclength coordinate. Thus, when the arclength decreases from 1 down to -1, the arclength coordinate in (*b*) increases from 1 to 3 (and then from 3 to 5 for those cases where the point vortex passes around the clamped end). We can see that ϵ drops considerably when the vortex reaches the free and clamped ends, and most but not all of the simulations end in those states.

In figure 7(*c*) and (*d*) we focus on the simulation corresponding to the dashed lines from (*a*) and (*b*) (and figure 6). In (*c*), we plot energies and energy fluxes during the simulation.

The finite part of the fluid kinetic energy, derived in appendix B, is

$$\widetilde{KE}_{fluid} = -\frac{1}{2\pi}\int_{-1}^{1} \gamma(s,t)\log|z_v - \zeta(s,t)|\,\mathrm{d}s - \frac{1}{4\pi}\int_{-1}^{1}\int_{-1}^{1} \gamma(s,t)\gamma(s',t)\log|\zeta(s,t) - \zeta(s',t)|\,\mathrm{d}s'\,\mathrm{d}s. \tag{4.4}$$

This is analogous to the finite part of the kinetic energy for a system of point vortices (Saffman 1992), and has the same form if the integrals are discretized and the term with $s = s'$ is omitted from the quadrature of (4.4). The rate of work done by the

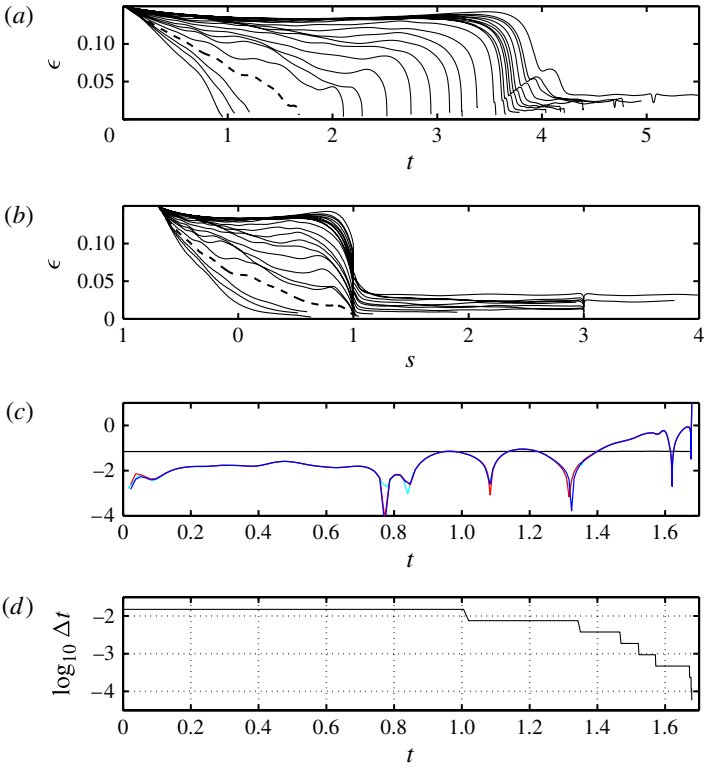

FIGURE 7. (Colour online) Separating distances, energy fluxes and time step during approaches of vortices to filaments. (*a*) The minimum distance from the vortex to the filament (ϵ), versus time, for filaments with 24 different values of R_2 ranging over three orders of magnitude. The values are 0.0042, 0.006, 0.0075, 0.01, 0.014, 0.02, 0.024, 0.03, 0.042, 0.06, 0.075, 0.1, 0.14, 0.2, 0.24, 0.3, 0.42, 0.6, 0.75, 1, 1.4, 2, 2.4 and 4.2. In each case $x_0 = 0.3$, $y_0 = 0.15$. (*b*) The values of ϵ from (*a*) now plotted with respect to the arclength location on the filament nearest to the vortex. The arclength is continued above 1 as the vortex travels around the free end of the filament. (*c*) For $R_2 = 0.01$, the dashed lines in (*a*) and (*b*), values of total energy and energy fluxes versus time. The horizontal line is $\log_{10}|\widetilde{KE}_{fluid} + U_{el}|$ (fluid kinetic energy plus elastic energy). The curved lines show $\log_{10}|\mathrm{d}\widetilde{KE}_{fluid}/\mathrm{d}t|$ (medium grey or red line), $\log_{10}|\mathrm{d}U_{el}/\mathrm{d}t|$ (dark grey or dark blue line), and $\log_{10}|P|$ (light grey or light blue line) (the rates of change of fluid kinetic energy and elastic energy and the rate of work done by the filament on the fluid). (*d*) For $R_2 = 0.01$, the logarithm, base 10, of the time step, versus time.

filament on the fluid is

$$P = \int_{-1}^{1} [p] v \, \mathrm{d}s, \tag{4.5}$$

and the elastic energy of the filament is

$$U_{el} = \frac{R_2}{2} \int_{-1}^{1} \kappa\,(s,t)^2 \, \mathrm{d}s. \tag{4.6}$$

In figure 7(*c*), the horizontal line is the sum of the elastic energy (4.6) and the finite part of the kinetic energy (4.4). The curved lines show $\log_{10}|\mathrm{d}\widetilde{KE}_{fluid}/\mathrm{d}t|$ (medium

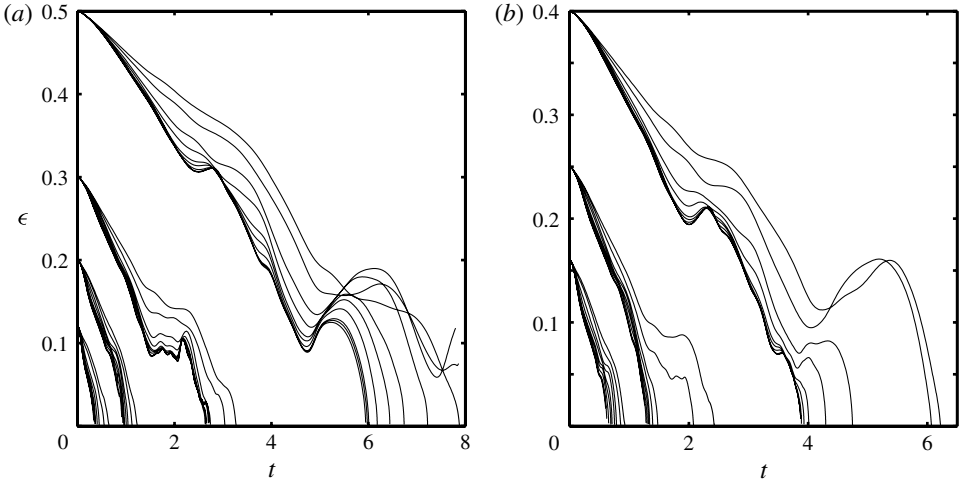

FIGURE 8. (*a*) Vortex filament distance versus time for $y_0 = 0.12$, 0.2, 0.3 and 0.5 and 10 values of $R_2 : 1, 2, 3\times10^{-5}$, $1, 2, 3, 6\times10^{-4}$ and $1, 2, 3\times10^{-3}$. In all cases, $x_0 = 0.3$. (*b*) Same data as in '(*a*)' but for $y_0 = 0.16$, 0.25 and 0.4.

grey or red line), $\log_{10}|\mathrm{d}U_{el}/\mathrm{d}t|$ (dark grey or dark blue line) and $\log_{10}|P|$ (light grey or light blue line). All of the lines agree well; on this logarithmic scale, noticeable disagreement only occurs for short time intervals when the quantities pass through zero. There are large spikes in the energy fluxes shortly before the end of the simulation. The total energy changes more rapidly during this time, but changes by less than 2 % up to the end of the simulation.

In figure 7(*d*) we plot the time step during the course of the simulation. The time step begins at 0.015, and is halved eight times during the simulation, as ϵ drops. Three of the halvings occur quite close to the end of the simulation, reflecting the sudden approach of the filament to the vortex.

We now consider much smaller values of R_2, and seven different values of y_0. At these combinations of R_2 and y_0, the simulations run up to smaller vortex–filament distances, which allows more information to be obtained about the dynamics when the vortex is close to the filament.

In figure 8, we show $\epsilon(t)$, as in figure 7(*a*), but now for more flexible filaments and seven different values of y_0. The curves are plotted on two separate panels to reduce overlapping. As in figure 7(*a*) (where y_0 was uniquely 0.15), the different curves emanating from each y_0 correspond to different values of R_2. Smaller R_2 again correspond to faster decreases in distance. The curves converge at the smallest R_2 $(1, 2, 3 \times 10^{-5})$; in these cases, the rigidity of the filament is negligible until the very end of the simulation, when the filament becomes very sharply bent, so at small rigidity, the dynamics are nearly the same over most of the simulation. In this limit, the filament behaves somewhat like a free surface with zero normal stress.

At the smallest y_0 (0.12, 0.16 and 0.2), the curves tend monotically to zero, and little more can be seen at the scale of this plot. At larger y_0 (0.3, 0.4 and 0.5) a more complicated dynamics, usually non-monotonic, is seen. Here the filament and point vortex move over a larger distance as they attract, and the increased time allows for more complicated dynamics.

In figure 9, we show the motion of the filament and vortex at the smallest value of R_2, 10^{-5}, and the largest value of y_0, 0.5, from figure 8. The filament moves rapidly

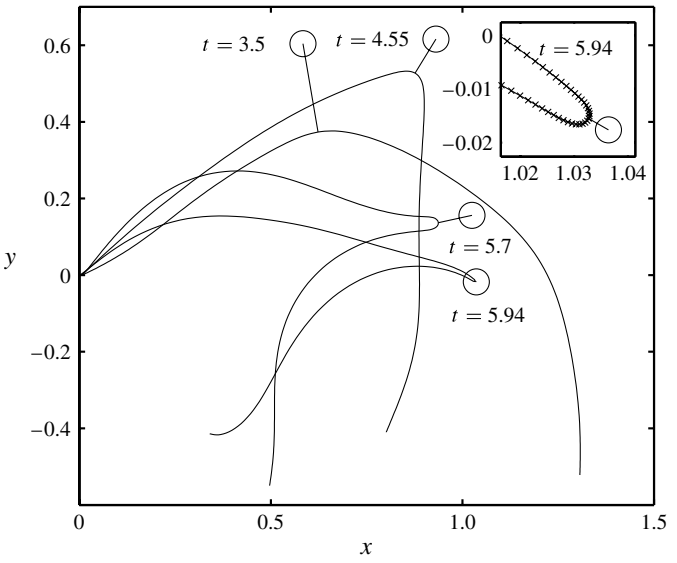

FIGURE 9. Snapshots of point vortex and filament for $R_2 = 10^{-5}$, $y_0 = 0.5$ and $x_0 = 0.3$. The inset shows a close-up near the vortex, and the spatial grid on the filament, at the final time.

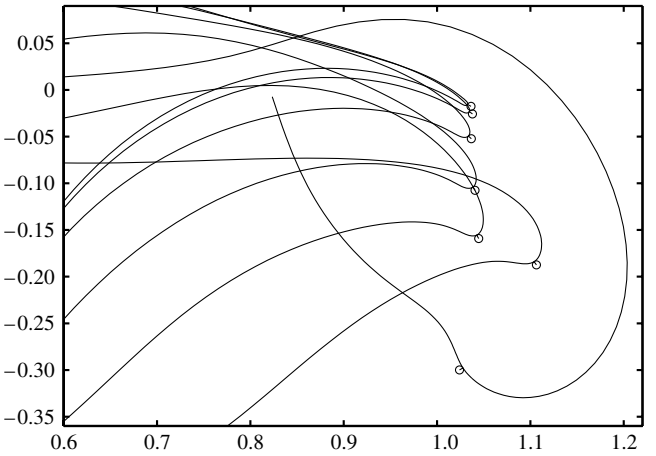

FIGURE 10. Positions of the filament and vortex when the distance between the two is 4.2×10^{-3}, for seven values of R_2 : $1, 3 \times 10^{-5}$, $1, 2, 3, 6 \times 10^{-4}$ and 3×10^{-3}. In all cases $y_0 = 0.5$ and $x_0 = 0.3$.

towards the point vortex throughout the simulation. The point vortex initially moves upward, somewhat away from the filament (y_v has increased to 0.6 at $t = 3.5$), but in general the point vortex moves roughly parallel to the tangent to the filament at its closest point. The filament becomes sharply curved at this point at later times (5.7 and 5.94), and protrudes as a sharpening finger towards the vortex.

In figure 10, we compare the positions of the filament and vortex for several small values of R_2 when the vortex has reached a certain distance from the filament (4.2×10^{-3}). At the two smallest R_2 values, the filaments are the most sharply curved and the positions of both the filaments and vortices are nearly the same. As R_2

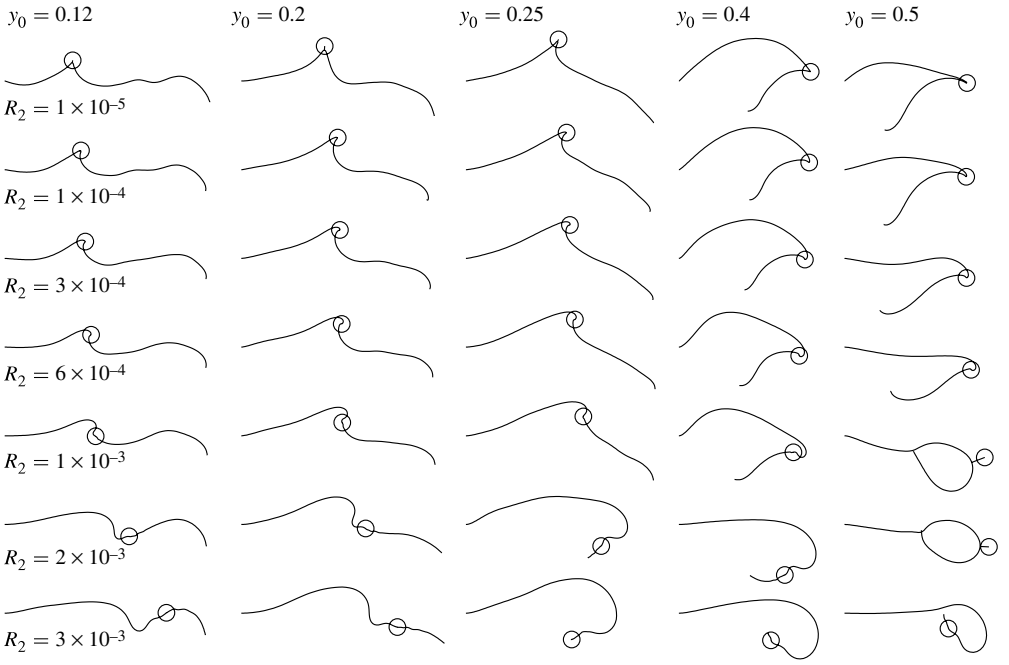

FIGURE 11. Positions of the filament and vortex at the end of the simulation for a matrix of five y_0 values and seven R_2 values, labelled at the top of each column and left-hand side of each row, respectively. In each case $x_0 = 0.3$.

increases, the shape of the filament near the vortex remains quite similar, curved downward toward the vortex, but with curvature decreased in each case. At the largest R_2 value, the position begins to show a more significant difference, with the vortex displaced tangentially forward from the location of maximum filament curvature.

We expand our comparison to many values of y_0 and R_2 in figure 11. In the first row ($R_2 = 10^{-5}$), the filament is bent most sharply. At smaller y_0 (left side of the figure), the filament moves directly upward to the vortex, which translates slightly to the right before the separation distance becomes very small. In the second row ($R_2 = 10^{-4}$), the shape of the filament is very similar, but more rounded and rotated clockwise near the vortex. This trend continues as R_2 increases to 3×10^{-4} and 6×10^{-4}. At $R_2 = 10^{-3}$, the vortex 'escapes' from the crest of the filament: it translates tangentially forward along the filament to a point of reversed curvature or 'trough'. At $R_2 = 2 \times 10^{-3}$ and $R_2 = 3 \times 10^{-3}$, it escapes the trough, and moves forward tangentially, nearing but not reaching the filament free end at the final time of the simulation. At $y_0 = 0.5$ and $R_2 = 10^{-3}$ and 2×10^{-3}, the filament free end nearly touches an interior point before the vortex gets very close to the filament. The simulation ends when the filament is close to self-contact (the distance from the end to the interior region is 7.7×10^{-3} for $R_2 = 10^{-3}$ and 1.4×10^{-2} for $R_2 = 2 \times 10^{-3}$). No special effort is made to cluster grid points in the self-contact region, and the grid points near the vortex are spaced at a distance 1.8×10^{-2} for $R_2 = 2 \times 10^{-3}$, so these two simulations are somewhat under-resolved at the final times.

For these very flexible filaments, the curves of figure 8 suggest that the vortex and filament collide at a finite time. In nearly all of these cases, the putative collision occurs at an interior point of the filament, away from the ends. We guess that the

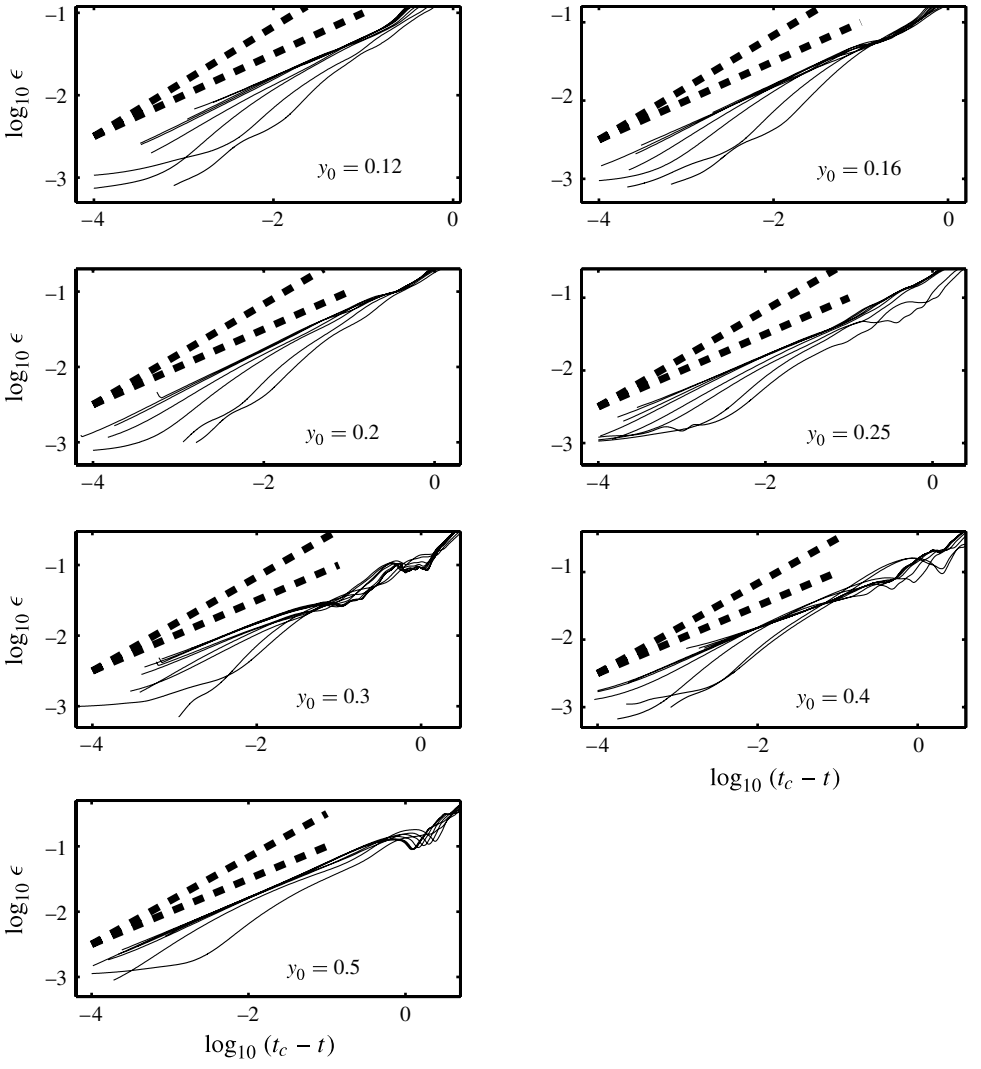

FIGURE 12. Log–log plot of the data from figure 8, with t_c chosen separately for each curve, as the value which makes the data most nearly linear over the last factor of 10 decrease in the minimum distance, on the log–log plot.

curves fit power laws of the form $A\,(t_c - t)^{\alpha}$ near collision times, t_c, which are unknown. For each curve in figure 8, we estimate t_c as the value which makes the plot of $\log_{10}\epsilon$ versus $\log_{10}(t_c - t)$ most nearly linear over the last factor of 10 decrease in ϵ. With these values of t_c, we replot the data from figure 8 on log–log scales in figure 12.

Many of the curves seem to fit a simple power law, but many do not. Those which do not are associated with a qualitative change in dynamics close to the end of the simulation. The most common examples are the snapshots in figure 11 where the vortices have escaped from the crest of the filament near the end of the simulation. This occurs less often at smaller R_2 values, and these values generally correspond to the straighter lines in figure 12. Other deviating examples are the filament self-collisions and cases where the point vortex is near the free end of the filament. The

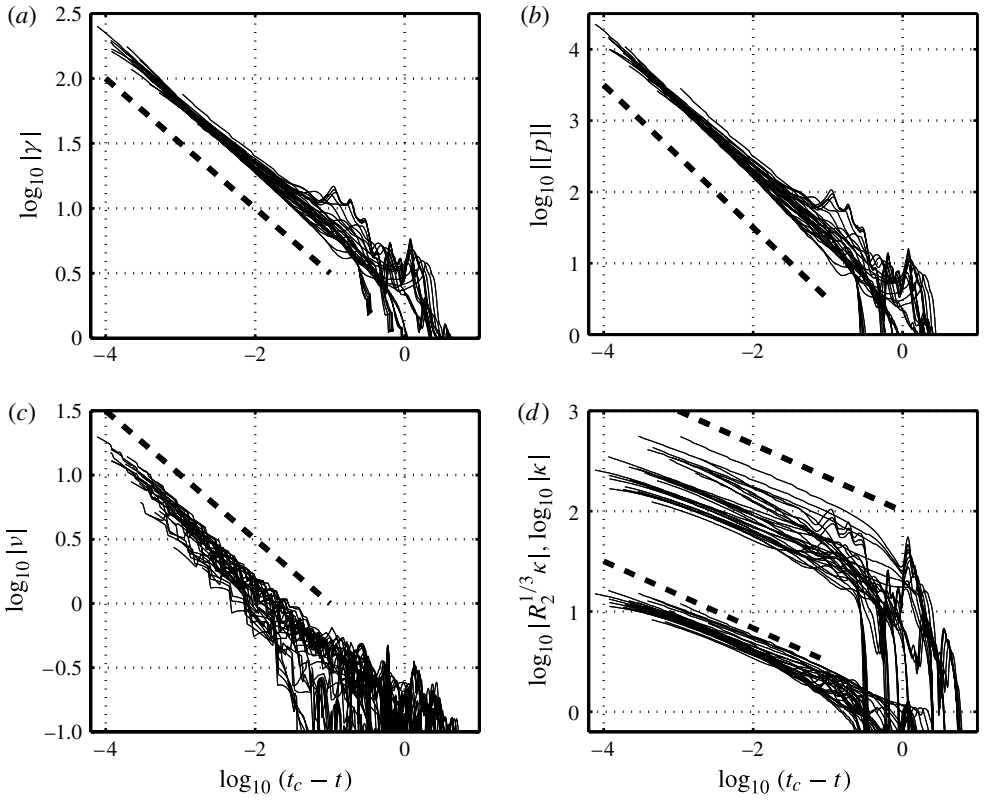

FIGURE 13. Plots of $\log_{10}|\gamma|$, $\log_{10}|[p]|$, $\log_{10}|\nu|$ and $\log_{10}|\kappa|$ at the point on the filament nearest to the vortex, for the simulations corresponding to data from 30 of the 70 curves in figures 8 and 12, with the same $\log_{10}(t_c - t)$ values as in figure 12. For the $|\kappa|$ data, the lower set of curves, below the lower dashed line, shows $\log_{10}|R_2^{1/3}\kappa|$.

curves which are most nearly linear in figure 12 are well fit by the power law

$$\epsilon(t) = O((t_c - t)^{1/2}), \tag{4.7}$$

which is shown by the lower of the two dashed lines in each figure. For comparison, the upper dashed line shows the power law $(t_c - t)^{2/3}$. Of the 70 curves plotted in figure 12 (10 in each of 7 frames), we select the 30 which are most nearly linear over the last factor of 10 decrease in ϵ. From the corresponding simulations, we collect the values of four key flow and shape quantities at the point on the filament nearest to the vortex, with arclength coordinate $s_v(t)$. The four quantities are γ, $[p]$, ν and κ. Each of the four panels of figure 13 shows the data for one of the four quantities, in the 30 selected simulations, on a log–log plot. We find that the four quantities are well fit by the following power laws, shown by the dashed lines in figure 13:

$$\gamma(s_v(t), t) = O((t_c - t)^{-1/2}), \quad [p](s_v(t), t) = O((t_c - t)^{-1}), \tag{4.8}$$

$$\nu(s_v(t), t) = O((t_c - t)^{-1/2}), \quad \kappa(s_v(t), t) = O((t_c - t)^{-1/3}). \tag{4.9}$$

We now attempt to explain the observed scalings. Again, let $\epsilon(t)$ denote the minimum distance from the vortex to a point on the filament, as a function of time,

and $s_v(t)$ denote the arclength coordinate of that nearest point on the filament. We now estimate quantities within $O(\epsilon)$ of the point vortex and $\zeta(s_v(t), t)$.

We first consider the kinematic equation (2.5), evaluated at s near $s_v(t)$. The second term on the left-hand side, which is the normal flow velocity induced by the point vortex, diverges as ϵ^{-1}. We can estimate v on the right-hand side by the following observation. The point vortex moves mainly tangentially to the filament, while the region of the filament near the vortex moves mainly normally to itself, towards the point vortex. The tangential motion of the point vortex is exact for an infinitely long, straight filament, and nearly exact in the close vicinity of a rigid filament (see figure 2). In our simulations, it moves nearly tangentially even for very deformed filaments, except near the end point singularities. Therefore, the change in the distance between the vortex and filament is almost entirely due to v, the normal motion of the filament:

$$v(s_v(t), t) \approx \frac{\mathrm{d}\epsilon}{\mathrm{d}t}. \tag{4.10}$$

Assuming that ϵ tends to zero as a power of $t_c - t$,

$$v(s_v(t), t) = O\left(\frac{\epsilon}{t_c - t}\right). \tag{4.11}$$

In the principal value integral of γ in (2.5), let us assume that the filament is smooth near the point vortex, so that the dominant, singular part of the kernel is a Cauchy kernel, independent of ϵ. Then, in the neighbourhood of s_v,

$$\gamma + O(\epsilon^{-1}) = O\left(\frac{\epsilon}{t_c - t}\right). \tag{4.12}$$

We now assume that all of the terms in (4.12) are important near the point vortex: all are of comparable magnitude. This implies that

$$\epsilon(t) = O((t_c - t)^{1/2}), \tag{4.13}$$

which agrees with figure 12 and

$$\gamma(s_v(t), t) = O((t_c - t)^{-1/2}), \tag{4.14}$$

which agrees with figure 13(*a*). Also, combining (4.13) with (4.11),

$$v(s_v(t), t) = O((t_c - t)^{-1/2}), \tag{4.15}$$

which agrees with figure 13(*c*).

We now consider the pressure jump (2.9), evaluated at $s = s_v(t)$. The equation was derived for a fixed arclength position s, but now we are assuming a moving arclength position $s_v(t)$. We may repeat the derivation of (2.9), given in appendix A, but with all quantities evaluated at $s = s_v(t)$. Equation (2.9) still applies, with all quantities evaluated at $s_v(t)$, and there is one additional change. In place of τ, which is $\partial_t \boldsymbol{X}(s, t) \cdot \hat{\boldsymbol{s}}$, we have

$$\frac{\mathrm{d}}{\mathrm{d}t}\boldsymbol{X}(s_v(t), t) \cdot \hat{\boldsymbol{s}}(s_v(t), t). \tag{4.16}$$

In other words, we replace τ with the tangential velocity of a point which moves along the filament to remain nearest to the point vortex. We recall the physical picture that the point vortex moves tangentially to the filament, while the filament

moves normally to itself, towards the point vortex. Then the quantity in (4.16) is approximately the velocity of the point vortex. By (2.7), we can estimate the velocity of the point vortex. The dominant part of the integral is the $O(\epsilon)$ neighbourhood of s_v. There $\gamma \sim \epsilon^{-1}$, and the kernel $\sim\epsilon^{-1}$, but the length of integration $\sim\epsilon$. The point vortex velocity scales as the product of these three terms, which is $O(\epsilon^{-1})$.

The other terms in (2.9) can also be estimated near s_v. By the arguments already given, both terms on the right-hand side of (2.8) are $\sim\epsilon^{-1}$, so this is the size of μ. The characteristic length over which the quantities in (2.9) change is ϵ, so we approximate ∂_s by factors of ϵ^{-1}. Also, we again assume that all quantities are powers of $t_c - t$, so we replace ∂_t by a factor of $(t_c - t)^{-1}$. We finally obtain, in place of (2.9), the scaling relation

$$O(\epsilon^{-1}\,(t_c - t)^{-1}) + O(\epsilon^{-3}) = O([p]\epsilon^{-1}). \tag{4.17}$$

Using (4.13),

$$[p](s_v(t), t) = O((t_c - t)^{-1}) \tag{4.18}$$

which agrees with figure 13(*b*). Also, with this scaling for $[p]$ and ϵ, all of the terms in (4.17) are of comparable magnitude.

Now we turn to the beam equation (2.1), which simplifies to

$$R_2(\partial_{ss}\kappa + \tfrac{1}{2}\kappa^3) = [p]. \tag{4.19}$$

We have eliminated the tension from (2.1) by integrating the tangential component of (2.1) from the free end. The s-derivatives can be estimated by a multiplicative factor which is the inverse length scale over which κ changes. The flow changes over the length scale ϵ, but the shape of the filament (or its curvature κ) changes over the length scale $1/\kappa$. Then the two terms on the left-hand side of (4.19) both scale like κ^3, and using (4.18),

$$R_2^{1/3}\kappa = O((t_c - t)^{-1/3}). \tag{4.20}$$

In figure 13(*d*), we plot κ with and without the factor of $R_2^{1/3}$. The factor provides a good collapse of the data (clearly better than other powers of R_2 which differ non-trivially from $1/3$).

5. Conclusion and future directions

We have found attractive dynamics for point vortices near filaments with a wide range of rigidities. We have also determined the power law scalings characterizing the collisions of point vortices with flexible filaments. The vortex–filament distance tends to zero as a square root of temporal distance from the critical time.

We have used zero-thickness filaments partly because they are more tractable computationally than bodies of finite thickness. The filaments' sharp ends cause inverse square-root singularities in flow velocity and pressure, and can strongly attract the vortex when it becomes sufficiently close to the ends. In this work we have not focused on this interaction, because it is somewhat specialized. We have focused instead on the cases where the collision appears to occur on the interior of the filament, far from the sharp ends. However, we have also investigated a more physical treatment of the flow at the filament free end, which is to allow the shedding of a vortex sheet according to the unsteady Kutta condition (Alben 2009). In this case, as the point vortex approaches the free end, the shed vortex sheet winds around the point vortex (under the flow velocity it induces), forming a spiral. The point vortex remains

confined at the centre of the spiral, at least for a certain length of time. In general, we may expect vortex shedding from the flexible surface to modify the interaction, but the present work shows the attractive dynamics that occur before such vortex shedding events.

A potential area of application is fish swimming in vortex streets (Liao *et al.* 2003; Alben 2008*a*, 2010). The distal regions of individual fish fins are very flexible (Alben, Madden & Lauder 2007; Flammang, Alben & Lauder 2012) and may undergo large deformations under collisions with vortices, similar to those seen here (Lauder 2011; Tangorra, Gericke & Lauder 2011).

An intuitive explanation for the collision we have found here is that the point vortex induces a pressure jump on the filament which pulls the filament towards it. Meanwhile, the vortex translates in a direction roughly parallel to the filament. The attraction is strong enough to cause a finite-time collision, as occurs with particles under power-law attractive forces which are an inverse power of distance, such as point charges or dipoles. Here the pressure jump scales as an inverse power of distance (ϵ). However, rigid bodies can also be attracted to point vortices, but we are unaware of a case in which a collision occurs. The Hamiltonian structure of these systems does not preclude collisions, which can occur in systems of three point vortices (Aref 1979). A natural question for future work is to understand whether collisions are possible for a rigid body of general shape and a point vortex. Put differently, one may ask whether the transition from periodic dynamics to a finite-time collision occurs when the filament rigidity is changed from infinite to finite, or whether the transition occurs at some finite value of filament rigidity. We suspect the former case, since the dynamics are generally attractive, but have no definite answer yet.

A large class of open questions concerns the effects of finite vortex size and viscosity on the dynamics. Recent studies have considered interactions of vortex patches with rigid walls, and found complex filamentation of the vortices as they move along the wall and through gaps in walls (Johnson & McDonald 2005; Crowdy & Surana 2007). We hypothesize that the filamentation dynamics for flexible bodies would be qualitatively similar to that which occurs for rigid walls, but it is unclear specifically how the finite-time collision would be altered. Collisions of viscous vortices with rigid walls have been reviewed by Rockwell (1998), but little is known about the case in which the wall is flexible. Such is the case for many important biological structures (Combes & Daniel 2003; Wang 2005; Griffith *et al.* 2009; Miller & Peskin 2009).

Acknowledgements

We would like to acknowledge the support of the NSF Division of Mathematical Sciences (grant number 1022619).

A supplementary movie is available at http://dx.doi.org/10.1017/jfm.2012.78.

Appendix A. Pressure jump equation

Here we derive the equation for the pressure jump $[p]$ across the filament in terms of γ and other quantities. We will arrive at an expression similar to that given by Hou, Lowengrub & Shelley (1994). We use vector notation instead of complex notation, for simplicity.

The flow velocity $\boldsymbol{u}(\boldsymbol{x}, t)$ at a point $\boldsymbol{x}$ in the fluid evolves according to the Euler momentum equation:

$$\partial_t \boldsymbol{u}(\boldsymbol{x}, t) + \boldsymbol{u}(\boldsymbol{x}, t) \cdot \nabla \boldsymbol{u}(\boldsymbol{x}, t) = -\nabla p(\boldsymbol{x}, t). \tag{A 1}$$

We wish to calculate the fluid pressure at a point in the fluid that is adjacent to a material point $\boldsymbol{X}(s, t)$ on the filament. The rate of change of fluid velocity at such a point is given by

$$\frac{\mathrm{d}}{\mathrm{d}t}\boldsymbol{u}(\boldsymbol{X}(s, t), t) = \partial_t \boldsymbol{u}(\boldsymbol{x}, t)|_{\boldsymbol{x}=\boldsymbol{X}(s,t)} + \partial_t \boldsymbol{X} \cdot \nabla \boldsymbol{u}(\boldsymbol{x}, t)\Big|_{\boldsymbol{x}=\boldsymbol{X}(s,t)}. \tag{A 2}$$

Combining (A 1) and (A 2) gives the pressure gradient in terms of the flow speed at a point that moves with the filament:

$$\frac{\mathrm{d}}{\mathrm{d}t}\boldsymbol{u}(\boldsymbol{X}(s, t), t) + (\boldsymbol{u}(\boldsymbol{x}, t) - \partial_t \boldsymbol{X}) \cdot \nabla \boldsymbol{u}(\boldsymbol{x}, t)|_{\boldsymbol{x}=\boldsymbol{X}(s,t)} = -\nabla p(\boldsymbol{x}, t)|_{\boldsymbol{x}=\boldsymbol{X}(s,t)}. \tag{A 3}$$

We write (A 3) separately for points in the fluid on the two sides of the filament. We use $+$ to denote the side towards which the filament normal $\hat{\boldsymbol{n}}$ is directed, and $-$ for the other side of the filament:

$$\frac{\mathrm{d}}{\mathrm{d}t}\left(\boldsymbol{u}(\boldsymbol{X}(s, t), t)\right)^{\pm} + \left((\boldsymbol{u}(\boldsymbol{x}, t) - \partial_t \boldsymbol{X}) \cdot \nabla \boldsymbol{u}(\boldsymbol{x}, t)|_{\boldsymbol{x}=\boldsymbol{X}(s,t)}\right)^{\pm} = -\left(\nabla p(\boldsymbol{x}, t)|_{\boldsymbol{x}=\boldsymbol{X}(s,t)}\right)^{\pm}. \tag{A 4}$$

We now decompose the fluid velocity into its components tangent and normal to the filament. The component normal to the filament is the same as that of the filament normal velocity, v. We note that the vortex sheet strength is also the jump in the tangential component of fluid velocity, across the filament (Saffman 1992). We denote by μ the average of the tangential components of fluid velocity on the two sides of the filament, given in (2.8). We express the tangential ($\hat{\boldsymbol{s}}$) and normal ($\hat{\boldsymbol{n}}$) components of the fluid velocity on either side of the filament in terms of μ and v:

$$\boldsymbol{u}^{\pm} = \left(\mu \mp \frac{\gamma}{2}\right)\hat{\boldsymbol{s}} + v\hat{\boldsymbol{n}}. \tag{A 5}$$

We now take the difference of (A 4) on the plus and minus sides. Since the normal components of all terms are continuous across the body, only the tangential component of the difference is non-zero. The tangential component of the difference is

$$-\partial_t \gamma(s, t) + \hat{\boldsymbol{s}} \cdot [(\boldsymbol{u}(\boldsymbol{x}, t) - \partial_t \boldsymbol{X}) \cdot \nabla \boldsymbol{u}(\boldsymbol{x}, t)|_{\boldsymbol{x}=\boldsymbol{X}(s,t)}]^{+}_{-} = -\partial_s [p(s, t)]^{+}_{-} \tag{A 6}$$

Using (A 5) and (2.6) in vector form,

$$\partial_t \boldsymbol{X} = \tau\hat{\boldsymbol{s}} + v\hat{\boldsymbol{n}}, \tag{A 7}$$

the second term on the left-hand side of (A 6) is

$$\begin{aligned}\hat{\boldsymbol{s}} \cdot \left[\left(\mu - \frac{\gamma}{2} - \tau\right)\partial_s\left(\left(\mu - \frac{\gamma}{2}\right)\hat{\boldsymbol{s}} + v\hat{\boldsymbol{n}}\right) - \left(\mu + \frac{\gamma}{2} - \tau\right)\partial_s\left(\left(\mu + \frac{\gamma}{2}\right)\hat{\boldsymbol{s}} + v\hat{\boldsymbol{n}}\right)\right] \\ = -\partial_s((\mu - \tau)\gamma).\end{aligned} \tag{A 8}$$

Inserting this expression into (A 6), we obtain (2.9) for the pressure jump:

$$\partial_t \gamma + \partial_s((\mu - \tau)\gamma) = \partial_s [p]^{+}_{-}. \tag{A 9}$$

For simplicity, we denote the pressure jump elsewhere as $[p]$ (i.e. we drop the $^{+}_{-}$).

Appendix B. Fluid kinetic energy

The total fluid kinetic energy can be written in terms of the stream function ψ:

$$KE_{fluid} = \lim_{\eta\to 0}\lim_{R\to\infty}\frac{1}{2}\iint_{D=\{z:\eta<|z-z_v|<R,z\notin\{\zeta(s),-1\leqslant s\leqslant 1\}\}} |\nabla\psi|^2\,\mathrm{d}A \tag{B 1}$$

$$= \frac{1}{2}\oint_{filament}\psi\,\partial_n\psi\,\mathrm{d}s + \frac{1}{2}\lim_{\eta\to 0}\oint_{|z-z_v|=\eta}\psi\,\partial_n\psi\,\mathrm{d}s$$
$$+\frac{1}{2}\lim_{R\to\infty}\oint_{|z-z_v|=R}\psi\,\partial_n\psi\,\mathrm{d}s. \tag{B 2}$$

The area integral in (B 1) is over an annular domain, centred at the point vortex, which excludes the filament. In the limits given, the domain grows to include the entire flow field outside of the point vortex and filament. Writing the integral as a limit allows us to decompose the energy into infinite terms, and finite terms which depend on the configuration of the filament and vortex, as in Saffman (1992). The normal coordinate n increases moving outward from the domain D. The integrals in (B 2) are around the boundaries of the annulus and the filament. The integral around the filament is

$$\frac{1}{2}\oint_{filament}\psi\,\partial_n\psi\,\mathrm{d}s = \frac{1}{2}\int_{-1}^{1}\psi\,(\partial_n\psi^+ + \partial_n\psi^-)\,\mathrm{d}s \tag{B 3}$$

where $+$ and $-$ denote the plus and minus sides of the filament, as defined below (2.9). Using the Cauchy–Riemann equation relating ψ to the velocity potential ϕ,

$$\partial_n\psi^\pm = \mp\partial_s\phi^\pm = \mp\hat{\boldsymbol{s}}\cdot\boldsymbol{u}^\pm, \tag{B 4}$$

where s is the arclength coordinate for the filament. Thus,

$$\frac{1}{2}\oint_{filament}\psi\,\partial_n\psi\,\mathrm{d}s = -\frac{1}{2}\int_{-1}^{1}\psi\,[\hat{\boldsymbol{s}}\cdot\boldsymbol{u}]_-^+\,\mathrm{d}s = \frac{1}{2}\int_{-1}^{1}\psi\gamma\,\mathrm{d}s. \tag{B 5}$$

The stream function at a point z in the flow is

$$\psi = -\frac{1}{2\pi}\log|z-z_v| - \frac{1}{2\pi}\int_{-1}^{1}\gamma(s,t)\log|z-\zeta(s,t)|\,\mathrm{d}s. \tag{B 6}$$

Inserting (B 6), evaluated on the filament, into (B 5),

$$\frac{1}{2}\oint_{filament}\psi\,\partial_n\psi\,\mathrm{d}s = -\frac{1}{4\pi}\int_{-1}^{1}\gamma(s,t)\log|z_v-\zeta(s,t)|\,\mathrm{d}s$$
$$-\frac{1}{4\pi}\int_{-1}^{1}\int_{-1}^{1}\gamma(s,t)\gamma(s',t)\log|\zeta(s,t)-\zeta(s',t)|\,\mathrm{d}s'\,\mathrm{d}s. \tag{B 7}$$

On the small circle $z = z_v + \eta\mathrm{e}^{\mathrm{i}\varphi}$,

$$\partial_n\psi = \frac{1}{2\pi\eta} + \mathrm{Re}\left(\frac{\mathrm{e}^{\mathrm{i}\varphi}}{2\pi}\int_{-1}^{1}\frac{\gamma(s,t)\,\mathrm{d}s}{z-\zeta(s)}\right). \tag{B 8}$$

On the large circle $z = z_v + R\mathrm{e}^{\mathrm{i}\varphi}$,

$$\partial_n\psi = -\frac{1}{2\pi R} - \mathrm{Re}\left(\frac{\mathrm{e}^{\mathrm{i}\varphi}}{2\pi}\int_{-1}^{1}\frac{\gamma(s,t)\,\mathrm{d}s}{z-\zeta(s)}\right). \tag{B 9}$$

The total circulation around the body is zero, so the total circulation in the flow is that of the point vortex, which is unity in our dimensionless units. Therefore, ψ and $\partial_n\psi$ have the following expansions far from the point vortex:

$$\psi = -\frac{1}{2\pi}\log R + O\left(\frac{1}{R}\right), \quad \partial_n\psi = -\frac{1}{2\pi R} + O\left(\frac{1}{R^2}\right), \quad R \gg 1. \tag{B 10}$$

Therefore,

$$\frac{1}{2}\oint_{|z-z_v|=R} \psi\,\partial_n\psi\,\mathrm{d}s = \frac{1}{4\pi}\log R + O(1), \quad R \gg 1. \tag{B 11}$$

Using ψ and $\partial_n\psi$ near the point vortex (B 6) and (B 8),

$$\frac{1}{2}\oint_{|z-z_v|=\eta} \psi\,\partial_n\psi\,\mathrm{d}s = -\frac{1}{4\pi}\log\eta - \frac{1}{4\pi}\int_{-1}^{1}\gamma(s,t)\log|z_v-\zeta(s,t)|\,\mathrm{d}s + O(1), \quad \eta \ll 1. \tag{B 12}$$

We sum (B 7) and the second term in (B 12) to obtain the finite part of the kinetic energy:

$$\widetilde{KE}_{fluid} = -\frac{1}{2\pi}\int_{-1}^{1}\gamma(s,t)\log|z_v-\zeta(s,t)|\,\mathrm{d}s - \frac{1}{4\pi}\int_{-1}^{1}\int_{-1}^{1}\gamma(s,t)\gamma(s',t)\log|\zeta(s,t)-\zeta(s',t)|\,\mathrm{d}s'\,\mathrm{d}s. \tag{B 13}$$

This is the same as (4.4).

REFERENCES

AKHTAR, I., MITTAL, R., LAUDER, G. V. & DRUCKER, E. 2007 Hydrodynamics of a biologically inspired tandem flapping foil configuration. *Theor. Comput. Fluid Dyn.* **21** (3), 155–170.

ALBEN, S. 2008*a* On the swimming of a flexible body in a vortex street. *J. Fluid Mech.* **635**, 27–45.

ALBEN, S. 2008*b* Optimal flexibility of a flapping appendage at high Reynolds number. *J. Fluid Mech.* **614**, 355–380.

ALBEN, S. 2009 Simulating the dynamics of flexible bodies and vortex sheets. *J. Comput. Phys.* **228** (7), 2587–2603.

ALBEN, S. 2009 Wake-mediated synchronization and drafting in coupled flags. *J. Fluid Mech.* **641**, 489–496.

ALBEN, S. 2010 Passive and active bodies in vortex-street wakes. *J. Fluid Mech.* **642**, 95–125.

ALBEN, S. 2011 Interactions between vortices and flexible walls. *Intl J. Non Linear Mech.* **46**, 586–591.

ALBEN, S., MADDEN, P. G. & LAUDER, G. V. 2007 The mechanics of active fin-shape control in ray-finned fishes. *J. Roy. Soc. Interface* **4** (13), 243–256.

AREF, H. 1979 Motion of three vortices. *Phys. Fluids* **22**, 393–400.

BEAL, D. N., HOVER, F. S., TRIANTAFYLLOU, M. S., LIAO, J. C. & LAUDER, G. V. 2006 Passive propulsion in vortex wakes. *J. Fluid Mech.* **549**, 385–402.

BORISOV, A. V., MAMAEV, I. S. & RAMODANOV, S. M. 2007 Dynamic interaction of point vortices and a two-dimensional cylinder. *J. Math. Phys.* **48**, 065403.

BOYD, J. P. 2001 *Chebyshev and Fourier Spectral Methods*. Dover.

COMBES, S. A. & DANIEL, T. L. 2003 Flexural stiffness in insect wings II. Spatial distribution and dynamic wing bending. *J. Exp. Biol.* **206** (17), 2989–2997.

CROWDY, D. & MARSHALL, J. 2006 The motion of a point vortex through gaps in walls. *J. Fluid Mech.* **551** (1), 31–48.

CROWDY, D. & SURANA, A. 2007 Contour dynamics in complex domains. *J. Fluid Mech.* **593** (1), 235–254.

DOLIGALSKI, T. L., SMITH, C. R. & WALKER, J. D. A. 1994 Vortex interactions with walls. *Annu. Rev. Fluid Mech.* **26** (1), 573–616.

DRUCKER, E. G. & LAUDER, G. V. 2001 Locomotor function of the dorsal fin in teleost fishes: experimental analysis of wake forces in sunfish. *J. Exp. Biol.* **204** (17), 2943–2958.

ELDREDGE, J. D. & PISANI, D. 2008 Passive locomotion of a simple articulated fish-like system in the wake of an obstacle. *J. Fluid Mech.* **607**, 279–288.

FLAMMANG, B. E., ALBEN, S. & LAUDER, G. V. 2012 Vortex perturbation of fish hovering. In *Integrative and Comparative Biology, 2012 Annual Meeting Abstracts*.

GRIFFITH, B. E., LUO, X., MCQUEEN, D. M. & PESKIN, C. S. 2009 Simulating the fluid dynamics of natural and prosthetic heart valves using the immersed boundary method. *Intl J. Appl. Mech.* **1** (1), 137–177.

HOU, T. Y., LOWENGRUB, J. S. & SHELLEY, M. J. 1994 Removing the stiffness from interfacial flows with surface tension. *J. Comput. Phys.* **114** (2), 312–338.

JOHNSON, E. R. & MCDONALD, N. R. 2005 Vortices near barriers with multiple gaps. *J. Fluid Mech.* **531**, 335–358.

KADTKE, J. B. & NOVIKOV, E. A. 1993 Chaotic capture of vortices by a moving body. I. The single point vortex case. *Chaos* **3**, 543.

KANSO, EVA & OSKOUEI, B. G. 2008 Stability of a coupled body–vortex system. *J. Fluid Mech.* **600**, 77–94.

KATZ, J. & PLOTKIN, A. 2001 *Low-speed Aerodynamics*. Cambridge University Press.

LAUDER, G. V. 2011 Swimming hydrodynamics: ten questions and the technical approaches needed to resolve them. *Exp. Fluids* **51** (1), 23–35.

LIAO, J. C., BEAL, D. N., LAUDER, G. V. & TRIANTAFYLLOU, M. S. 2003 Fish exploiting vortices decrease muscle activity. *Science* **302** (5650), 1566–1569.

MANELA, A. & HOWE, M. S. 2009 The forced motion of a flag. *J. Fluid Mech.* **635**, 439–454.

MILLER, L. A. & PESKIN, C. S. 2009 Flexible clap and fling in tiny insect flight. *J. Expl Biol.* **212** (19), 3076.

MILNE-THOMSON, L. M. 1968 *Theoretical Hydrodynamics*, 5th edn. Macmillan.

PROTAS, B. 2008 Vortex dynamics models in flow control problems. *Nonlinearity* **21**, R203.

RISTROPH, L. & ZHANG, J. 2008 Anomalous hydrodynamic drafting of interacting flapping flags. *Phys. Rev. Lett.* **101** (19), 194502.

ROCKWELL, D. 1998 Vortex-body interactions. *Ann. Rev. Fluid Mech.* **30** (1), 199–229.

ROENBY, J. & AREF, H. 2010 Chaos in body–vortex interactions. *Proc. R. Soc.* A **466** (2119), 1871.

SAFFMAN, P. 1992 *Vortex Dynamics*. Cambridge University Press.

SHASHIKANTH, B. N., MARSDEN, J. E., BURDICK, J. W. & KELLY, S. D. 2002 The Hamiltonian structure of a two-dimensional rigid circular cylinder interacting dynamically with N point vortices. *Phys. Fluids* **14**, 1214.

STREITLIEN, K., TRIANTAFYLLOU, G. S. & TRIANTAFYLLOU, M. S. 1996 Efficient foil propulsion through vortex control. *AIAA J.* **34** (11), 2315–2319.

TANGORRA, J. L., GERICKE, T. & LAUDER, G. V. 2011 Learning from the fins of ray-finned fish for the propulsors of unmanned undersea vehicles. *Mar. Technol. Soc. J.* **45** (4), 65–73.

VANKERSCHAVER, J., KANSO, E. & MARSDEN, J. E. 2009 The geometry and dynamics of interacting rigid bodies and point vortices. *J. Geom. Mech.* **1**, 223–266.

WANG, Z. J. 2005 Dissecting insect flight. *Annu. Rev. Fluid Mech.* **37**, 183–210.